Multimodal characterization of the bone-implant interface using Raman spectroscopy and nanoindentation

Manon Fraulob, Siyuan Pang, Sophie Le Cann, Romain Vayron, Mathilde Laurent-Brocq, Soorya Todatry, Julio A.N.T. Soares, Iwona Jasiuk, Guillaume Haiat

To cite this version:

Manon Fraulob, Siyuan Pang, Sophie Le Cann, Romain Vayron, Mathilde Laurent-Brocq, et al.. Multimodal characterization of the bone-implant interface using Raman spectroscopy and nanoindentation. Medical Engineering & Physics, 2020, 84, pp.60-67. 10.1016/j.medengphy.2020.07.013 . hal-02955104

HAL Id: hal-02955104
https://hal.science/hal-02955104v1

Submitted on 1 Oct 2020

Multimodal characterization of the bone-implant interface using Raman spectroscopy and nanoindentation

Manon Fraulob[a], Siyuan Pang[b], Sophie Le Cann[a], Romain Vayron[a], Mathilde Laurent-Brocq[c], Soorya Todatry[b], Julio A.N.T. Soares[d], Iwona Jasiuk[b], Guillaume Haïat[a]*

[a] *CNRS, Laboratoire Modélisation et Simulation Multi Echelle, MSME UMR CNRS 8208, France*

[b] *Department of Mechanical Science and Engineering, University of Illinois at Urbana-Champaign, USA*

[c] *CNRS, Univ Paris Est Créteil, ICMPE, UMR7182, 94320 Thiais, France*

[d] *Materials Research Laboratory, University of Illinois at Urbana-Champaign, USA*

*** CORRESPONDING AUTHOR:**

Guillaume Haiat
Laboratoire Modélisation et Simulation Multi Echelle (MSME), Equipe Biomécanique
Université Paris-Est Créteil Val de Marne (UPEC), Faculté des Sciences et Technologie
61, Avenue du Général de Gaulle 94010 Créteil Cedex - FRANCE
E-mail: Guillaume.HAIAT@cnrs.fr

Keywords: Bone tissue, implant, Raman spectroscopy, nanoindentation, osseointegration

Abstract. Titanium implants are widely used in dental and orthopedic surgeries. Osseointegration phenomena lead to direct contact between bone tissue and the implant surface. The quality of the bone-implant interface (BII), resulting from the properties of newly formed bone, determines the implant stability. This study investigates the BII properties using a dedicated *in vivo* implant model consisting of a coin-shaped Ti-6Al-4V implant inserted in a rabbit femur for 10 weeks. A gap created around the implant was filled with newly formed bone tissue after healing. The properties of mature and newly formed bone tissue were compared using: i) Raman spectroscopy to assess the nanoscale compositional bone properties and ii) nanoindentation to quantify microscale elastic properties in site-matched regions. The mineral-to-matrix ratio, crystallinity (mineral size and lattice order), and the collagen cross-link ratio were significantly lower in newly formed bone tissue (e.g., a mineral-to-matrix ratio of 9.3 ± 0.5 for proline 853 cm^{-1}) compared to mature bone (15.6 ± 1). Nanoindentation measurements gave Young's modulus of 12.8 ± 1.8 GPa for newly formed bone and 15.7 ± 2.3 GPa for mature bone. This multimodal and multiscale approach leads to a better understanding of osseointegration phenomena.

Doi 10.1016/j.medengphy.2020.07.013

1. Introduction

Titanium implants are widely used in orthopedic and dental surgeries, and their long-term stability relies on successful osseointegration phenomena during the healing period. Periprosthetic bone tissue forms and remodels at the bone-implant interface (BII) to achieve direct contact with the implant, adapting the tissue properties to the implant mechanical environment. The properties of this newly formed bone tissue are key for the surgical success of the implant, which clinically translates to a long-term stability [1]. Specifically, implant stability depends on the bone quantity (amount of bone) and bone quality (mechanical properties, biochemical composition, and structure of bone tissue) in a region of interest located at a distance less than about 200 µm from the implant surface [2]. Incomplete osseointegration or degradation of the bone properties (quantity and quality) at the BII during healing could ultimately lead to a lack of stability and implant failure and require a new surgery for the patient [3]. Therefore, a better understanding of the evolution of the BII properties during healing is essential for the prediction of surgical outcomes [4].

Various animal studies have been carried out to investigate the properties of newly formed bone tissue around clinical implants [2]. However, the complex geometry of commercial implants leads to multiaxial stress distribution at the BII, making it challenging to understand the determinants of osseointegration phenomena. Thus, we used an *in vivo* implant model with a planar interface [5-9] to work under more reproducible and standardized conditions. A coin-shaped implant model was designed, based on prior studies [5, 10, 11], including a gap of several hundred micrometers below the implant surface. Initially empty, the corresponding volume was filled with bone tissue during healing, thus allowing, unlike in clinical implants, to clearly distinguish between mature and newly formed bone [11-16].

The evaluation of the BII properties is complicated due to the multiscale and composite nature of bone and its constant evolution [17]. Bone mass consists of around 70% of inorganic phase and 30% of organic phase by weight. The inorganic phase is a mineral made of hydroxyapatite ($Ca_5(PO_4)_3OH$) crystals, while the organic phase contains collagen (mainly type I), non-collagenous proteins, and lipids [17-19]. The bone has a highly hierarchical structure. At the scale of tens of nanometres, the collagen molecule is a triple helix made of three polypeptides, which are chains of amino acids [20] such as phenylalanine, proline, and hydroxyproline (formed from proline). At the scale of hundreds of nanometres, the mineralized collagen molecules are grouped into bundles forming fibrils, stabilized by cross-links [20, 21]. Surrounded by extrafibrillar crystals, fibrils assemble into fibers to form the bone ultrastructure at a scale of 1–10 µm [22].

Because of the hierarchical structure of bone tissue, a multimodal and multiphysics methodology is necessary to study biomechanical properties of bone [2, 3, 22, 23]. Nanoindentation has been used to measure the microscale elastic properties of the BII at dental implants [24, 25] to assess the effect of implant material and surface treatment [24, 26, 27], mechanical loading [28], and bone maturation and healing [27, 29]. The differences in elastic properties between the newly formed bone tissue and pre-existing mature bone have been characterized around a titanium plate [30] and around the aforementioned coin-shaped implants [13, 16]. Quantitative ultrasound techniques such as micro-Brillouin scattering [11] and echographic analyses [15] have also been used to obtain information on the biomechanical properties of the BII. Torsion tests were carried out to measure the effective adhesion energy of the BII [14]. However, to the best of our knowledge, the relationship between the microscopic mechanical properties of newly formed bone tissue around an implant and its biochemical composition, including mineral crystals and collagen structures, has not been studied.

Raman spectroscopy is an attractive technique to evaluate the local bone tissue biochemical composition at the nanoscale, which includes the mineral (hydroxyapatite) and organic (collagen components, non-collagenous proteins, and other organics) phases. Raman spectroscopy has been used to characterize the effects of metabolic disorders on bone tissue [31-33] and to investigate the remodeling process of healing bone tissues [34, 35]. Some studies have characterized bone tissue remodeling in the surroundings of composite biomaterials [36, 37] or titanium implants [38, 39]. However, these studies did not allow to distinguish between mature and newly formed bone tissue clearly.

This study aims to develop a multimodal and multiphysics approach to investigate the microscopic mechanical and compositional properties of periprosthetic bone tissue. Thus, Raman spectroscopy and nanoindentation are used in site-matched regions of interest, in mature and newly formed bone tissues, using a dedicated animal model by inserting a coin-shaped titanium implant in a rabbit femur for 10 weeks.

2. Methods

2.1. Implants

A Ti-6Al-4V coin-shaped implant (diameter of 5 mm, length of 3 mm), blasted with titanium dioxide particles (average surface roughness Ra = 1.9 µm), was surrounded by a polytetrafluoroethylene (PTFE) cap to avoid bone tissue growth around the implant and create a 750 µm gap underneath the implant, to host new bone tissue (see Fig. 1).

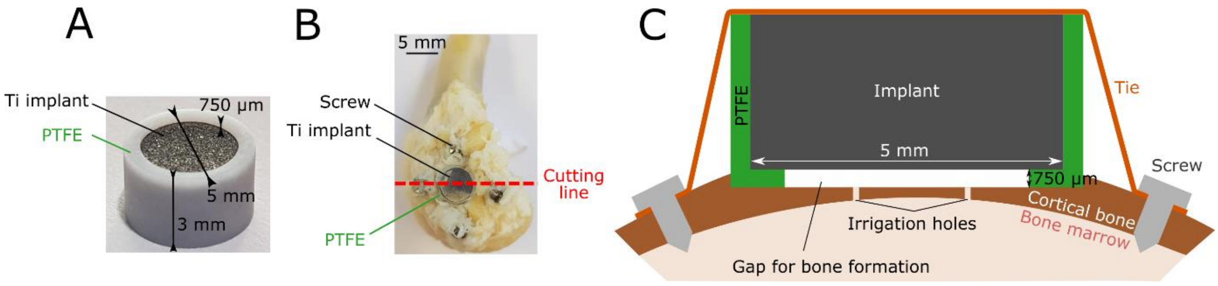

Figure 1: A: Photograph of a coin-shaped implant surrounded by a PTFE cap prior to surgery. B: Sample with the implant inserted in the distal-medial portion of the femur. C: Schematic description of the cross-sectional view of the coin-shaped implant model.

2.2. *Surgical procedure*

The implantation protocol has been detailed in previous work [11]. A New Zealand white rabbit (> 3.5 kg) was anesthetized, and a 5 cm longitudinal incision was made to expose the distal-medial part of the right femur (Fig. 1B). The periosteum was incised to expose the implantation site. A 5.6 mm diameter (Ø) hole was drilled to level the bone surface (Zimmer, Palm Beach Gardens, FL, USA) as well as four irrigation holes through the cortex (Ø 0.9 mm) to allow blood flow towards the interface. To stabilize the implant, four holes (Ø 1.2 mm) were drilled around the central hole to receive Ø 1.6 mm screws, connected by two orthodontic elastic strings (Easy Implant, Chavanod, France). Animal handling was approved by the ethical committee of ENVA (École Nationale Vétérinaire d'Alfort) and followed the requirements of *The European Guidelines for Care and Use of Laboratory Animals*. After 10 weeks of healing time, the rabbit was euthanized with an overdose of pentobarbital, and the distal femur (3 cm-long) was carefully dissected with the implant in place (Fig. 1B).

2.3. *Sample preparation*

The sample was embedded in polymethyl methacrylate (PMMA) in order to be able to cut it. The sample was fixed for 1 week in 10 % phosphate-buffered formalin, rinsed with water, dehydrated in ethanol, cleared in xylene, and finally embedded in methyl methacrylate (MMA) [40, 41].

The embedded sample was cut transversally through the middle of the implant (Fig. 1B) with a low-speed cut-off machine (Minitom, Struers®, Ballerup, Denmark) and the distal part of the sample was analyzed. The surface of interest was manually polished (LabPol-5, Struers®, Ballerup, Denmark) using abrasive paper, SiC foil with grit 1200, and polishing cloths with 9-µm alumina powder and then 0.3-µm alumina suspension. Next, Raman spectroscopy measurements were collected on the sample surface, as described in subsection 2.4. Non-decalcified histology was done to distinguish mature and newly formed bone tissue. Finally, nanoindentation measurements were carried out, as described in subsection 2.5.

2.4. Raman spectroscopy

Raman spectroscopy was realized using a model RAMAN-11 confocal Raman microscope (Nanophoton, Osaka, Japan). A 785 nm (infrared light) laser with 1 mW power was used for beam excitation. The scattered light reflects compositions of mineral and collagen phases due to the difference in molecule and ion vibrations. The sample was scanned through a 20×/0.45 objective with 100 s exposure time. Six lines were measured: three in newly formed bone tissue (labeled a, b, c in Fig. 2) and three in mature bone tissue (d, e, f in Fig. 2). Each measured line extended over 400 μm (pixel size 1 μm), leading to a total of 400 spectra per line.

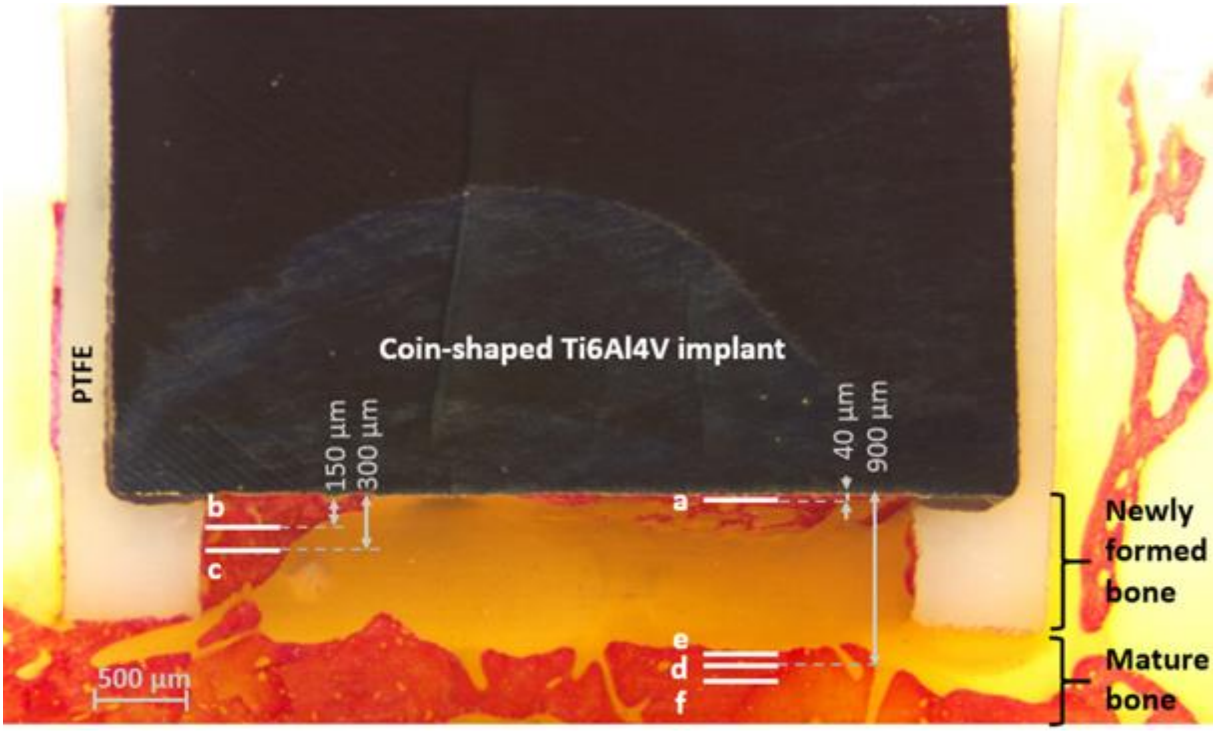

Figure 2: Histological image of the sample colored using van Gieson picro-fuchsin to expose bone tissue (red). The white lines correspond to the 400 μm long lines where Raman measurements were carried out: (a, b, c) in newly formed bone tissue and (d, e, f) in mature bone tissue. Nanoindentation was performed in site-matched regions of interest, see Fig. 4 for detailed locations.

The spectra intensity was measured between 400 and 1800 cm^{-1} [42]. The 400 spectra obtained for each line (Fig. 2) were averaged. All averaged spectra were then corrected by removing the baseline coming from fluorescence background by cubic spline interpolation. Eleven bands could be identified (Fig. 3), corresponding to bone tissue components from i) the mineral phase: phosphate bands ($\nu_1PO_4^{3-}$ and $\nu_2PO_4^{3-}$) and carbonate band ($\nu_1CO_2^{2-}$), and ii) the organic phase: amino acid (proline (Pro 853 and

Pro 920), hydroxyproline (Hyp), tyrosine (Tyr), phenylalanine (Phe)), collagen bands (amide I and amide III), and proteins bands with CH_2 deformation $\delta(CH_2)$.

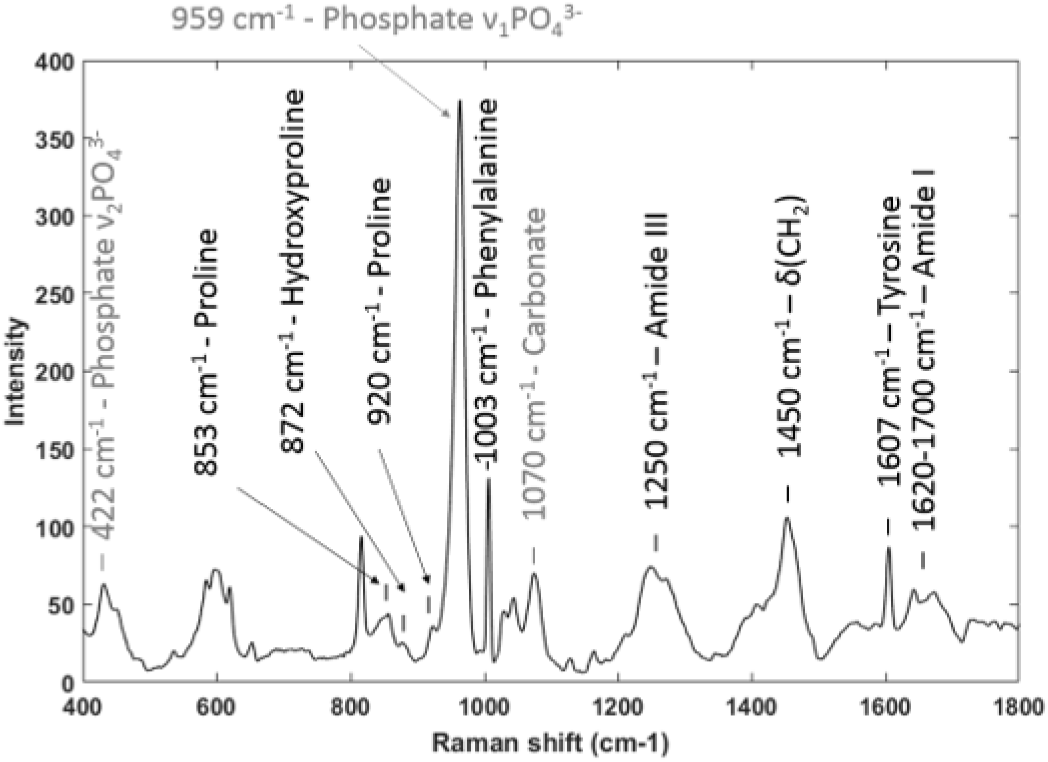

Figure 3: Average spectrum of line d (mature bone tissue) with characteristic bands of bone tissue components. The bands corresponding to the mineral (respectively organic) phase are indicated in grey (respectively black).

For each averaged spectrum, bands of interest were analyzed using Origin 2019b (OriginLab©, Northampton, USA). For each peak corresponding to the Raman shift *Y*, the area under the peak A_Y, the maximum intensity I_Y, and full width at half maximum $FWHM_Y$ were determined. Different parameters commonly used in Raman analyses [42, 43] were assessed (Table 1) for the six lines shown in Fig. 2. These parameters can be divided into three categories: indicators investigating the mineral phase (n=2), the organic phase (n=3), and the ratio of the mineral and organic phases (n=8).

Table 1: Raman parameters calculated for each average line. The subscript represents the peak position (cm^{-1}). *A*: area, *I*: maximum intensity, *FWHM*: full width at half maximum.

Raman parameters	**Ratios**	**Raman parameters**	**Ratios**
Mineral phase		**Mineral phase / Organic phase**	
Mineral crystallinity	$\frac{1}{FWHM_{959}}$	Mineral-to-matrix (Pro 853)	$\frac{I_{959}}{I_{853}}$
Carbonate-to-phosphate	$\frac{A_{1070}}{A_{959}}$	Mineral-to-matrix (Pro 853 + Hyp)	$\frac{I_{959}}{I_{853}+I_{872}}$
Organic phase		Mineral-to-matrix (Pro 853 + Hyp + Pro 920)	$\frac{I_{959}}{I_{853}+I_{872}+I_{920}}$
Phenylalanine-to-proline	$\frac{A_{1003}}{A_{853}}$	Mineral-to-matrix (δ(CH_2))	$\frac{I_{959}}{I_{1450}}$
Hydroxyproline-to-proline	$\frac{I_{872}}{I_{853}}$	Mineral-to-matrix (Phe)	$\frac{I_{959}}{I_{1003}}$
Amide I / Amide III	$\frac{I_{1620-1700}}{I_{1250}}$	Mineral-to-matrix (Tyr)	$\frac{I_{959}}{I_{1607}}$
		Carbonate-to-matrix	$\frac{A_{1070}}{A_{1620-1700}}$
		Calcium content	$\frac{A_{422}}{A_{1250}}$

2.5. Nanoindentation measurements

Nanoindentation was performed with a nanoindenter TI 950 TriboIndenter (Hysitron®, Minneapolis, USA) equipped with a diamond Berkovich tip. The sample was indented in Raman site-matched regions of interest (ROI), at room temperature and in dry conditions. Thirteen indents were done in newly formed bone tissue and nine in mature bone tissue (Fig. 4).

The indentation was load-controlled at a rate of 20 mN/s until a maximum force of 100 mN was reached, corresponding to approximately 3 µm of indentation depth. Then, the tip was maintained for a 2 s holding time and unloaded at 20 mN/s. A minimal distance of 70 µm between two indents was chosen to avoid interaction between the indented regions of interest (ROI) [44].

The bone tissue reduced modulus E_r was extracted from the unloading slope of the load-displacement curves [45]. Assuming that the bone tissue is a homogeneous, linear elastic, and isotropic material, the reduced modulus E_r is given as:

$$\frac{1}{E_r} = \frac{1-{v_b}^2}{E_b} + \frac{1-{v_i}^2}{E_i}, \qquad (1)$$

where E_b and v_b (respectively E_i and v_i) are Young's modulus and Poisson's ratio of bone (respectively diamond indentor tip). Values of $v_b = 0.3$, $E_i = 1141$ GPa, and $v_i = 0.07$ [24, 25, 27, 29] were used to determine the bone tissue elastic modulus E_b.

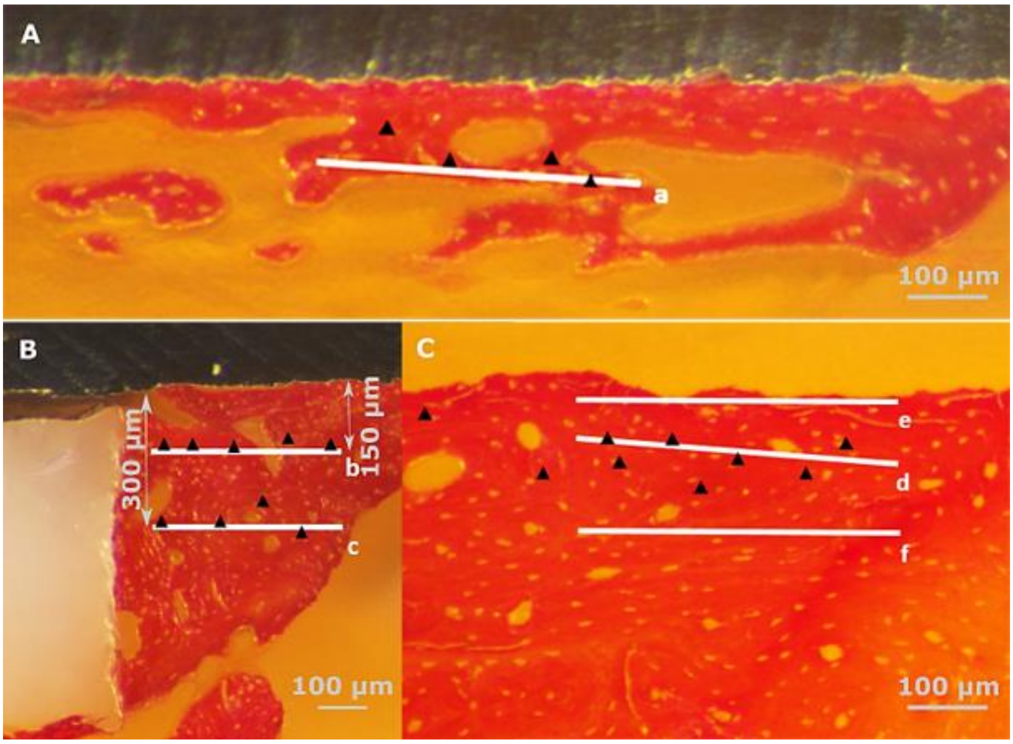

Figure 4: Locations of the nanoindentation measurement points (triangular points) in respect to the Raman measurements (white lines, see Fig. 2) in newly formed bone tissue (A, B) and mature bone tissue (C).

2.6. Statistical analysis

The results obtained with Raman spectroscopy and nanoindentation on mature and newly formed bone tissues were compared, considering the average and standard deviation values obtained in ROI lines d-f and ROI lines a-c, respectively. Due to the relatively small sample size, non-parametric Mann-Whitney U-tests were performed to assess a statistical significance between the newly formed and mature bone tissue values. The significance level was defined at p = 0.05.

3. Results

The results obtained for the different parameters derived from Raman spectroscopy and nanoindentation are shown in Table 2, which compares the values obtained for mature and newly formed bone tissue.

Table 2: Comparison between different parameters (mean ± standard deviation over the different ROI) derived from Raman spectroscopy and nanoindentation for mature and newly formed bone. Mann-Whitney U-test: * = parameters with significant p-values $p \leq 0.05$, ** = parameters with significant p-values $p \leq 0.01$.

Techniques	**Parameter**	**Mean and standard deviation for newly formed bone tissue**		**Mean and standard deviation for mature bone tissue**
Raman spectroscopy: Mineral phase	Mineral crystallinity	0.0590 ± 0.0007	</≈	0.0595 ± 0.0001
	Carbonate-to-phosphate *	0.391 ± 0.029	>	0.320 ± 0.020
Raman spectroscopy: Organic phase	Phenylalanine-to-proline *	1.100 ± 0.084	<	1.434 ± 0.136
	Hydroxyproline-to-proline *	0.377 ± 0.042	<	0.562 ± 0.030
	Amide I / Amide III *	0.373 ± 0.014	<	0.520 ± 0.067
Raman spectroscopy: Mineral phase / Organic phase	Mineral-to-matrix (Pro 853) *	9.298 ± 0.534	<	15.605 ± 1.006
	Mineral-to-matrix (Pro 853 + Hyp) *	6.758 ± 0.434	<	9.983 ± 0.482
	Mineral-to-matrix (Pro 853 + Hyp + Pro 920) *	4.932 ± 0.322	<	6.742 ± 0.064
	Mineral-to-matrix ($\delta(CH_2)$) *	2.873 ± 0.292	<	5.707 ± 1.115
	Mineral-to-matrix (Phe) *	2.083 ± 0.007	<	3.139 ± 0.079
	Mineral-to-matrix (Tyr) *	5.085 ± 0.478	<	7.213 ± 1.360
	Mineral-to-matrix (Amide III) "Calcium content"	0.406 ± 0.036	</≈	0.421 ± 0.026
	Carbonate-to-matrix *	2.780 ± 0.320	>	1.560 ± 0.104
Nanoindentation	Young's modulus E_b **	12.8 ± 1.8 GPa	<	15.7 ± 2.3 GPa

For the mineral phase, the mineral crystallinity is not significantly different between mature and newly formed bone tissue, while the carbonate-to-phosphate ratio is significantly higher for newly formed bone tissue. Moreover, the standard deviation of mineral crystallinity is seven times higher for the newly formed bone tissue.

All parameters representing the organic phase, i.e., phenylalanine-to-proline, hydroxyproline-to-proline, and amide I-to-amide III ratios, are significantly lower in the newly formed bone tissue compared to mature bone tissue.

All parameters related to the mineral-to-matrix ratios ($\nu_1PO_4^{3-}$/Pro 853, $\nu_1PO_4^{3-}$/(Pro 853 + Hyp), $\nu_1PO_4^{3-}$/(Pro 853 + Hyp + Pro 920), $\nu_1PO_4^{3-}/\delta(CH_2)$, $\nu_1PO_4^{3-}$/Phe and $\nu_1PO_4^{3-}$/Tyr), representative of the amount of the mineral phase relative to organic phase, are significantly lower in the newly formed bone tissue compared to mature bone tissue. Moreover, the carbonate-to-matrix ratio is significantly higher, and its standard deviation is three times higher for the newly formed bone tissue. The calcium content $\nu_2PO_4^{3-}$/Amide III is higher in the mature than in the newly formed bone tissue without being significantly different.

The elastic modulus of the newly formed bone tissue measured by nanoindentation is significantly lower than that obtained for mature bone tissue.

4. Discussion

A multimodal and multiphysics experimental approach, combining Raman spectroscopy and nanoindentation, was conducted to investigate the local compositional and mechanical properties of the newly formed bone tissue around an endosseous implant, which constitutes the originality of the present study.

4.1. Comparison with the literature

Young's moduli values measured in this study are of the same order of magnitude as those obtained in previous studies on rabbit bone [13, 46, 47]. The Young's modulus of newly formed bone found herein (12.8 ± 1.8 GPa) is slightly lower than the values obtained in [13], which may be due to the following reasons. First, the nanoindentation measurement technique was different since Vayron et al. [13] utilized a dynamic mode using a continuous stiffness measurement (CSM) technique, while the static mode was considered here. Second, we assumed a Poisson's ratio of bone tissue equal to 0.3, while Vayron et al. [13] used a value of 0.25. Note that assuming a value of 0.25 for the Poisson's ratio would have led to values of Young's modulus of newly formed bone tissue of 13.2 ± 1.9 GPa, closer to those found in [13]. Based on the literature [25, 26, 29, 48, 49], assuming a value of 0.3 for the Poisson's ratio seems to be more realistic compared to 0.25. We found that Young's modulus of mature bone tissue is equal to 15.7 ± 2.3 GPa, which is in agreement with other nanoindentation studies on rabbit bone [46, 47], which reported Young's moduli of mature bone between 9 and 18 GPa. Concerning Raman spectroscopy, all measured Raman ratios were of the same order of magnitude as in previous studies [31-35, 39] as detailed hereafter.

4.2. Evolution of the bone mineral composition

Bone tissue mineral characteristics were assessed through the mineral crystallinity and the carbonate-to-phosphate ratio. At the atomic scale, a low mineral crystallinity corresponds to small mineral crystals and reduced stoichiometric (lattice) perfection [35], while higher crystallinity implies more mature and elongated crystals. The higher standard deviation of the mineral crystallinity in newly formed bone tissue indicates more heterogeneity in crystal sizes, which can be explained by different mineralization stages.

The higher carbonate-to-phosphate ratio measured in newly formed bone tissue indicates that carbonate ions from the mineral phase are incorporated into the apatite lattice, leading to the substitution of the carbonate groups into the phosphate groups of hydroxyapatite crystals [35]. Such a phenomenon changes the atomic structure of crystals, affecting their size, solubility, and thermal stability, enabling easier apatite remodeling [50]. Likewise, active bone remodeling has been previously observed in bone tissue healing of a subcalvarial defect [35], and a decrease in carbonate substitution has been linked to an increase of mineral crystallinity in synthetic carbonated apatites [51]. Another indicator of bone remodeling is the carbonate-to-matrix ratio describing the evolution of carbonate minerals relative to amide I from the collagen matrix. Its significantly higher value in the newly formed bone tissue with a high standard deviation could also be explained by carbonate substitution and different remodeling stages [52].

4.3. Immature organic phase within newly formed bone

The difference between the composition of the organic phases of mature and newly formed bone tissue was investigated by considering the ratios of the different collagen components at the nanoscale. The amide I/amide III ratio gives a collagen cross-link ratio, which impacts mechanical properties, such as tensile strength and viscoelasticity [19]. A higher ratio of amide I/amide III means higher ratio of mature (nonreducible) to immature (reducible) collagen cross-links [42, 53]. The lower hydroxyproline-to-proline and amide I/amide III ratios found for newly formed bone tissue indicate a less mature tissue [34]. A lower ratio $\nu_1PO_4^{3-}$/Phe in newly formed bone tissue than mature bone tissue suggests a decrease of phenylalanine during osseointegration making phenylalanine in newly formed bone's extracellular matrix a sign of non-mature tissue, as seen around a 3D printed implant and after tooth extraction [34, 39].

The difference in composition between mature and newly formed bone tissues was assessed by quantifying the mineral content relative to the organic phase. The $\nu_1PO_4^{3-}$ phosphate band is generally accepted as the best indicator for the mineral phase. However, different organic constituents have been previously used to describe the matrix phase [42]: proline bands at 853 cm^{-1} and 920 cm^{-1} as well as hydroxyproline band at 872 cm^{-1} [34, 39, 54], but also amino acids such as phenylalanine [34, 39] and tyrosine [39] or proteins with CH_2 deformation band [33, 35, 55]. In the present study, all mineral-to-matrix ratio combinations reported in the literature appear to be consistently lower in newly formed than in mature bone tissue. Thus, the newly formed bone is composed of less mineral relative to matrix components, indicating lower mineralization and potential bone tissue maturation in process at the BII [33-35, 39, 54, 55]. Eventually, the mineral-to-matrix $\nu_2PO_4^{3-}$/Amide III ratio, an indicator of calcium content [52], has lower values in newly formed bone tissue, as previously observed for bone maturation [56], bone healing [34], and osseointegration of a 3D printed titanium implant [39].

4.4. *Effects of compositional and structural changes on bone's elastic properties*

Bone tissue compositional analysis was complemented with nanoindentation measurements to assess the microscale bone tissue elastic properties. The difference in properties of mature and newly formed bone can be related to the difference in mineralization obtained with Raman spectroscopy since the lower elastic modulus corresponds to a less mineralized tissue [13, 48, 57, 58]. In particular, the lower amount of mineral (low mineral-to-matrix ratios) and lower crystallinity (crystal size and lattice order) lead to lower elastic modulus [31, 59] and reduced strength [34, 59] of bone. Moreover, the bone tissue remodeling activity evidenced in newly formed bone tissue (high carbonate-to-phosphate and carbonate-to-matrix ratios) creates vacancies resulting in microstrains within the matrix of mature bone [54].

4.5. *Limitations of the study*

Only one sample was considered in the present study, which is justified for the following reasons. First, the coin-shaped implant model used here has already been validated in previous studies [11, 13, 16], which showed that this model allowed to clearly distinguish newly formed bone and mature bone. In a previous nanoindentation study [13], the standard deviation of Young's modulus of newly formed bone tissue within the bone chamber was equal to 1.81 GPa (respectively 1.55 GPa and 2.10 GPa) after 4 weeks of healing (respectively 7 and 13 weeks). A similar standard deviation equal to 1.8 GPa was obtained herein. Although interspecimen variability is expected, we assume that the relative difference between mature and newly formed bone is expected to be similar for distinct samples. Note that only one sample per healing time was also considered in [13]. Second, the sample was stained with van Gieson picro-fuchsin to confirm that the three lines of nanoindentation measurements were actually performed in newly formed bone tissue. Third, the nanoindentation apparatus was carefully calibrated with fused silica, and the Raman spectroscopy instrument has been used in previous studies [60, 61] so that both techniques have been validated. Fourth, a high number of Raman measurements were done to ensure a reliable description of bone compositional changes. Specifically, six lines of interest and 400 Raman spectra per line were considered, whereas other Raman studies on bone characterization [33-35, 38, 54] only considered tens of spectra for each sample. In the future, more samples could be analyzed to further investigate the correlation between mechanical and compositional parameters and the effect of healing time.

Another limitation lies in the sample preparation with the commonly used PMMA embedding resin [13, 27, 29, 30], which can affect the results [62]. Nonetheless, embedding is necessary to enable slicing of the sample to expose the interface and minimize damage due to cutting in the presence of the titanium implant. We focused on the relative differences between mature and newly formed bone tissues, thus limiting the impact of the sample preparation.

Conclusions

The multimodal and multiphysics experimental approach coupled with the dedicated *in vivo* model represents a powerful strategy to investigate the properties of newly formed bone tissue around the BII. The composition and structure of newly formed bone show a lower mineral content, lower crystallinity, lower collagen cross-link ratio, and higher remodeling rate compared to mature bone. These characteristics explain the lower elastic properties compared to mature bone tissue. The results indicate that changes in the bone composition and structure affect bone's mechanical properties while osseointegration occurs. Identifying and explaining the changes in bone tissue mechanical, compositional, and structural properties over healing time around metallic implants is essential to better understand the determinants of implant stability, leading to surgical success.

Acknowledgments

This project has received funding from the European Research Council (ERC) under the European Union's Horizon 2020 research and innovation program (grant agreement No 682001, project ERC

Consolidator Grant 2015 BoneImplant). This project has also received funding from the European Union's Horizon 2020 research and innovation programme under the Marie Sklodowska-Curie grant agreement No 797764. This research was also partially supported by the National Science Foundation grant DMR 15-07169 (IJ).

The experiments described in this work were carried out in part in the Materials Research Laboratory Central Facilities University of Illinois at Urbana-Champaign.

References

[1] Albrektsson T, Branemark PI, Hansson HA, Lindstrom J. Osseointegrated titanium implants. Requirements for ensuring a long-lasting, direct bone-to-implant anchorage in man. Acta orthopaedica Scandinavica. 1981;52:155-70.

[2] Haiat G, Wang HL, Brunski J. Effects of biomechanical properties of the bone-implant interface on dental implant stability: from in silico approaches to the patient's mouth. Annu Rev Biomed Eng. 2014;16:187-213.

[3] Gao X, Fraulob M, Haiat G. Biomechanical behaviours of the bone-implant interface: a review. J R Soc Interface. 2019;16:20190259.

[4] Winter W, Heckmann SM, Weber HP. A time-dependent healing function for immediate loaded implants. J Biomech. 2004;37:1861-7.

[5] Ronold HJ, Ellingsen JE. The use of a coin shaped implant for direct in situ measurement of attachment strength for osseointegrating biomaterial surfaces. Biomaterials. 2002;23:2201-9.

[6] Ronold HJ, Ellingsen JE. Effect of micro-roughness produced by TiO_2 blasting-tensile testing of bone attachment by using coin-shaped implants. Biomaterials. 2002;23:4211-9.

[7] Ronold HJ, Lyngstadaas SP, Ellingsen JE. A study on the effect of dual blasting with TiO_2 on titanium implant surfaces on functional attachment in bone. J Biomed Mater Res A. 2003;67:524-30.

[8] Ronold HJ, Ellingsen JE, Lyngstadaas SP. Tensile force testing of optimized coin-shaped titanium implant attachment kinetics in the rabbit tibiae. J Mater Sci Mater Med. 2003;14:843-9.

[9] Ronold HJ, Lyngstadaas SP, Ellingsen JE. Analysing the optimal value for titanium implant roughness in bone attachment using a tensile test. Biomaterials. 2003;24:4559-64.

[10] Wennerberg A, Jimbo R, Stubinger S, Obrecht M, Dard M, Berner S. Nanostructures and hydrophilicity influence osseointegration: a biomechanical study in the rabbit tibia. Clin Oral Implants Res. 2014;25:1041-50.

[11] Mathieu V, Fukui K, Matsukawa M, Kawabe M, Vayron R, Soffer E, et al. Micro-Brillouin scattering measurements in mature and newly formed bone tissue surrounding an implant. J Biomech Eng. 2011;133:021006.

[12] Vayron R, Barthel E, Mathieu V, Soffer E, Anagnostou F, Haiat G. Variation of biomechanical properties of newly formed bone tissue determined by nanoindentation as a function of healing time. Comput Methods Biomech Biomed Engin. 2011;14:139-40.

[13] Vayron R, Barthel E, Mathieu V, Soffer E, Anagnostou F, Haiat G. Nanoindentation measurements of biomechanical properties in mature and newly formed bone tissue surrounding an implant. J Biomech Eng. 2012;134:021007.

[14] Mathieu V, Vayron R, Barthel E, Dalmas D, Soffer E, Anagnostou F, et al. Mode III cleavage of a coin-shaped titanium implant in bone: effect of friction and crack propagation. J Mech Behav Biomed Mater. 2012;8:194-203.

[15] Mathieu V, Vayron R, Soffer E, Anagnostou F, Haiat G. Influence of healing time on the ultrasonic response of the bone-implant interface. Ultrasound Med Biol. 2012;38:611-8.

[16] Vayron R, Matsukawa M, Tsubota R, Mathieu V, Barthel E, Haiat G. Evolution of bone biomechanical properties at the micrometer scale around titanium implant as a function of healing time. Phys Med Biol. 2014;59:1389-406.

[17] Gao X, Sevostianov I. Connection between elastic and electrical properties of cortical bone. J Biomech. 2016;49:765-72.

[18] Olszta MJ, Cheng X, Jee SS, Kumar R, Kim YY, Kaufman MJ, et al. Bone structure and formation: A new perspective. Mater Sci Eng R: Reports. 2007;58:77-116.

[19] Paschalis EP, Verdelis K, Doty SB, Boskey AL, Mendelsohn R, Yamauchi M. Spectroscopic characterization of collagen cross-links in bone. J Bone Miner Res. 2001;16:1821-8.

[20] Kwansa AL, De Vita R, Freeman JW. Mechanical recruitment of N- and C-crosslinks in collagen type I. Matrix Biol. 2014;34:161-9.

[21] Unal M, Uppuganti S, Leverant CJ, Creecy A, Granke M, Voziyan P, et al. Assessing glycation-mediated changes in human cortical bone with Raman spectroscopy. J Biophotonics. 2018;11:e201700352.

[22] Shah FA, Thomsen P, Palmquist A. Osseointegration and current interpretations of the bone-implant interface. Acta Biomater. 2019;84:1-15.

[23] Palmquist A. A multiscale analytical approach to evaluate osseointegration. J Mater Sci Mater Med. 2018;29:60.

[24] Kim DG, Elias KL, Jeong YH, Kwon HJ, Clements M, Brantley WA, et al. Differences between buccal and lingual bone quality and quantity of peri-implant regions. J Mech Behav Biomed Mater. 2016;60:48-55.

[25] Yoon HI, Jeon MJ, Kim HL, Kim DG, Han JS. Spatial variation of bone biomechanical properties around a dental implant using nanoindentation: a case study. J Mech Behav Biomed Mater. 2018;79:168-72.

[26] Anchieta RB, Baldassarri M, Guastaldi F, Tovar N, Janal MN, Gottlow J, et al. Mechanical property assessment of bone healing around a titanium-zirconium alloy dental implant. Clin Implant Dent Relat Res. 2014;16:913-9.

[27] Johnson TB, Siderits B, Nye S, Jeong YH, Han SH, Rhyu IC, et al. Effect of guided bone regeneration on bone quality surrounding dental implants. J Biomech. 2018;80:166-70.

[28] Anchieta RB, Guimaraes MVM, Suzuki M, Tovar N, Bonfante EA, Atria P, et al. Nanomechanical assessment of bone surrounding implants loaded for 3 Years in a canine experimental model. J Oral Maxillofac Surg. 2018;76:71-9.

[29] Kim DG, Kwon HJ, Jeong YH, Kosel E, Lee DJ, Han JS, et al. Mechanical properties of bone tissues surrounding dental implant systems with different treatments and healing periods. Clin Oral Investig. 2016;20:2211-20.

[30] Claffey N, Bashara H, O'Reilly P, Polyzois I. Evaluation of new bone formation and osseointegration around subperiosteal titanium implants with histometry and nanoindentation. Int J Oral Maxillofac Implants. 2015;30:1004-10.

[31] Imbert L, Auregan JC, Pernelle K, Hoc T. Mechanical and mineral properties of osteogenesis imperfecta human bones at the tissue level. Bone. 2014;65:18-24.

[32] Kim G, Cole JH, Boskey AL, Baker SP, van der Meulen MC. Reduced tissue-level stiffness and mineralization in osteoporotic cancellous bone. Calcif Tissue Int. 2014;95:125-31.

[33] Pascart T, Falgayrac G, Migaud H, Quinchon JF, Norberciak L, Budzik JF, et al. Region specific Raman spectroscopy analysis of the femoral head reveals that trabecular bone is unlikely to contribute to non-traumatic osteonecrosis. Sci Rep. 2017;7:97.

[34] Shah FA, Sayardoust S, Thomsen P, Palmquist A. Extracellular matrix composition during bone regeneration in the human dental alveolar socket. Bone. 2019:244-9.

[35] Ahmed R, Law AWL, Cheung TW, Lau C. Raman spectroscopy of bone composition during healing of subcritical calvarial defects. Biomed Opt Express. 2018;9:1704-16.

[36] Borkowski L, Sroka-Bartnicka A, Polkowska I, Pawlowska M, Palka K, Zieba E, et al. New approach in evaluation of ceramic-polymer composite bioactivity and biocompatibility. Anal Bioanal Chem. 2017;409:5747-55.

[37] Sroka-Bartnicka A, Kimber JA, Borkowski L, Pawlowska M, Polkowska I, Kalisz G, et al. The biocompatibility of carbon hydroxyapatite/beta-glucan composite for bone tissue engineering studied with Raman and FTIR spectroscopic imaging. Anal Bioanal Chem. 2015;407:7775-85.

[38] Lopes CB, Pinheiro AL, Sathaiah S, Da Silva NS, Salgado MA. Infrared laser photobiomodulation (lambda 830 nm) on bone tissue around dental implants: a Raman spectroscopy and scanning electronic microscopy study in rabbits. Photomed Laser Surg. 2007;25:96-101.

[39] Shah FA, Snis A, Matic A, Thomsen P, Palmquist A. 3D printed Ti6Al4V implant surface promotes bone maturation and retains a higher density of less aged osteocytes at the bone-implant interface. Acta Biomater. 2016;30:357-67.

[40] Soffer E, Ouhayoun JP, Meunier A, Anagnostou F. Effects of autologous platelet lysates on ceramic particle resorption and new bone formation in critical size defects: the role of anatomical sites. J Biomed Mater Res B Appl Biomater. 2006;79:86-94.

[41] Chevallier N, Anagnostou F, Zilber S, Bodivit G, Maurin S, Barrault A, et al. Osteoblastic differentiation of human mesenchymal stem cells with platelet lysate. Biomaterials. 2010;31:270-8.

[42] Mandair GS, Morris MD. Contributions of Raman spectroscopy to the understanding of bone strength. Bonekey Rep. 2015;4:620.

[43] Morris MD, Mandair GS. Raman assessment of bone quality. Clin Orthop Relat Res. 2011;469:2160-9.

[44] Yang B, Vehoff H. Dependence of nanohardness upon indentation size and grain size - A local examination of the interaction between dislocations and grain boundaries. Acta Mater. 2007;55:849-56.

[45] Oliver WC, Pharr GM. Measurement of hardness and elastic modulus by instrumented indentation: Advances in understanding and refinements to methodology. J Mater Res. 2004;19:3-20.

[46] Anesi A, Ferretti M, Cavani F, Salvatori R, Bianchi M, Russo A, et al. Structural and ultrastructural analyses of bone regeneration in rabbit cranial osteotomy: Piezosurgery versus traditional osteotomes. J Craniomaxillofac Surg. 2018;46:107-18.

[47] Bianchi M, Boi M, Sartori M, Giavaresi G, Lopomo N, Fini M, et al. Nanomechanical mapping of bone tissue regenerated by magnetic scaffolds. J Mater Sci Mater Med. 2015;26:5363.

[48] Willems NM, Mulder L, den Toonder JM, Zentner A, Langenbach GE. The correlation between mineralization degree and bone tissue stiffness in the porcine mandibular condyle. J Bone Miner Metab. 2014;32:29-37.

[49] Pathak S, Vachhani SJ, Jepsen KJ, Goldman HM, Kalidindi SR. Assessment of lamellar level properties in mouse bone utilizing a novel spherical nanoindentation data analysis method. J Mech Behav Biomed Mater. 2012;13:102-17.

[50] Wopenka B, Pasteris JD. A mineralogical perspective on the apatite in bone. Mater Sci Eng C. 2005;25:131-43.

[51] Awonusi A, Morris MD, Tecklenburg MM. Carbonate assignment and calibration in the Raman spectrum of apatite. Calcif Tissue Int. 2007;81:46-52.

[52] Ciubuc JD, Manciu M, Maran A, Yaszemski MJ, Sundin EM, Bennet KE, et al. Raman spectroscopic and microscopic analysis for monitoring renal osteodystrophy signatures. Biosensors (Basel). 2018;8:1-11.

[53] Takahata M, Maher JR, Juneja SC, Inzana J, Xing L, Schwarz EM, et al. Mechanisms of bone fragility in a mouse model of glucocorticoid-treated rheumatoid arthritis: implications for insufficiency fracture risk. Arthritis and rheumatism. 2012;64:3649-59.

[54] Bi X, Patil CA, Lynch CC, Pharr GM, Mahadevan-Jansen A, Nyman JS. Raman and mechanical properties correlate at whole bone- and tissue-levels in a genetic mouse model. J Biomech. 2011;44:297-303.

[55] Marin C, Papantonakis G, Sels K, van Lenthe GH, Falgayrac G, Vangoitsenhoven R, et al. Unraveling the compromised biomechanical performance of type 2 diabetes- and Roux-en-Y gastric bypass bone by linking mechanical-structural and physico-chemical properties. Sci Rep. 2018;8:5881.

[56] Zhang HY, Zeng QF, Bai SP, Wang JP, Ding XM, Xuan Y, et al. Study on the morphology and mineralization of the tibia in meat ducks from 1 to 56 d. Poult Sci. 2019;98:3355-64.

[57] Sansalone V, Naili S, Bousson V, Bergot C, Peyrin F, Zarka J, et al. Determination of the heterogeneous anisotropic elastic properties of human femoral bone: from nanoscopic to organ scale. J Biomech. 2010;43:1857-63.

[58] Sansalone V, Bousson V, Naili S, Bergot C, Peyrin F, Laredo JD, et al. Anatomical distribution of the degree of mineralization of bone tissue in human femoral neck: impact on biomechanical properties. Bone. 2012;50:876-84.

[59] Yerramshetty JS, Akkus O. The associations between mineral crystallinity and the mechanical properties of human cortical bone. Bone. 2008;42:476-82.

[60] Su FY, Pang S, Ling YTT, Shyu P, Novitskaya E, Seo K, et al. Deproteinization of cortical bone: Effects of different treatments. Calcif Tissue Int. 2018;103:554-66.

[61] Pang S, Su FY, Green A, Salim J, McKittrick J, Jasiuk I. Demineralization of cortical bone using several protocols and synthesis of a collagen scaffold. Arch Biochem Eng. 2019;1:01-.

[62] Fiedler IAK, Casanova M, Keplinger T, Busse B, Muller R. Effect of short-term formaldehyde fixation on Raman spectral parameters of bone quality. J Biomed Opt. 2018;23:116504.